

M DWARF ACTIVITY IN THE PAN-STARRS 1 MEDIUM-DEEP SURVEY:
FIRST CATALOG AND ROTATION PERIODS

E. KADO-FONG¹, P. K. G. WILLIAMS², A. W. MANN^{3,4,5}, E. BERGER², W. S. BURGETT⁶, K. C. CHAMBERS⁶, M. E. HUBER⁶, N. KAISER⁶, R.-P. KUDRITZKI⁶, E. A. MAGNIER⁶, A. REST⁷, R. J. WAINSCOAT⁶, C. WATERS⁶

(Dated: February 12, 2018)

¹Department of Physics and Astronomy, Tufts University, Medford, MA 02155, USA

²Harvard-Smithsonian Center for Astrophysics, 60 Garden Street, Cambridge, MA 02138, USA

³The University of Texas at Austin, Department of Astronomy, 2515 Speedway C1400, Austin, TX 78712, USA

⁴Institute for Astrophysical Research, Boston University, 725 Commonwealth Ave, Boston, MA 02215, USA

⁵Harlan J. Smith Fellow

⁶Institute for Astronomy, University of Hawaii at Manoa, Honolulu, HI 96822, USA

⁷Space Telescope Science Institute, 3700 San Martin Drive, Baltimore, MD 21218, USA

ABSTRACT

We report on an ongoing project to investigate activity in the M dwarf stellar population observed by the Pan-STARRS 1 Medium Deep Survey (PS1-MDS). Using a custom-built pipeline, we refine an initial sample of ~ 4 million sources in PS1-MDS to a sample of 184,148 candidate cool stars using color cuts. Motivated by the well-known relationship between rotation and stellar activity, we use a multi-band periodogram analysis and visual vetting to identify 271 sources that are likely rotating M dwarfs. We derive a new set of polynomials relating M dwarf PS1 colors to fundamental stellar parameters and use them to estimate the masses, distances, effective temperatures, and bolometric luminosities of our sample. We present a catalog containing these values, our measured rotation periods, and cross-matches to other surveys. Our final sample spans periods of $\lesssim 1$ –130 days in stars with estimated effective temperatures of ~ 2700 –4000 K. Twenty-two of our sources have X-ray cross-matches, and they are found to be relatively X-ray bright as would be expected from selection effects. Our data set provides evidence that *Kepler*-based searches have not been sensitive to very slowly-rotating stars ($P_{\text{rot}} \gtrsim 70$ d), implying that the observed emergence of very slow rotators in studies of low-mass stars may be a systematic effect. We also see a lack of low-amplitude ($< 2\%$) variability in objects with intermediate (10–40 d) rotation periods, which, considered in conjunction with other observational results, may be a signpost of a loss of magnetic complexity associated with a phase of rapid spin-down in intermediate-age M dwarfs. This work represents just a first step in exploring stellar variability in data from the PS1-MDS and, in the farther future, LSST.

1. INTRODUCTION

The magnetic activity of Sun-like and lower-mass stars increases with rotation until a “saturation” point is reached, past which activity becomes largely insensitive to rotation (Pallavicini et al. 1981; Vilhu 1984; James et al. 2000; Pizzolato et al. 2003; Reiners et al. 2009). The details of this rotation-activity relation do not change significantly at the transition to fully convective structure in the lowest-mass stars ($M < 0.35 M_{\odot}$; Chabrier & Baraffe 2000), and many fully convective stars exhibit significant magnetic fields (Johns-Krull & Valenti 1996; Kiraga & Stepien 2007; Reiners & Basri 2010; Wright et al. 2011). These are surprising results,

given that the dynamos of solar-type stars are believed to operate at the “tachocline,” the transition layer between the radiative core and convective outer envelope that, by definition, is not present in fully convective stars (Charbonneau 2014).

The magnetic dynamos of fully convective stars are still relatively poorly understood. Recent theoretical efforts have worked to explain the existence of significant magnetic activity via the effect of rotation and convective flows (Dobler et al. 2006; Browning 2008; Gastine et al. 2012; Yadav et al. 2015); because of this focus, observations of the fully convective rotation-activity relation serve to constrain and inform such models.

On the observational front, recent campaigns to measure rotation periods of both fully convective and solar-type stars have benefitted greatly from automated and

semi-automated period measurement techniques hinging upon the detection of variations in the source brightness of time series photometry due to periodic observations of starspots on the target star. Such studies have greatly informed our knowledge of the distribution of stellar rotation periods with respect to stellar mass (see, e.g. [McQuillan et al. 2014](#); [Newton et al. 2016](#)); however, systematic effects specific to each survey near the fully convective transition make it difficult to disentangle astrophysical trends from systematic ones.

Here we present measurements of the photometric rotation periods of 271 M dwarfs in the PanSTARRS-1 Medium Deep Survey (PS1-MDS) data set, using the multi-band Lomb-Scargle periodogram developed by [VanderPlas & Ivezić \(2015\)](#) to take advantage of information provided by the five-filter photometry provided by PS1-MDS. We additionally identify archival X-ray counterparts, which act as a probe of the magnetic activity, for 22 of the sources.

The outline of the paper is as follows. First we discuss the PS1-MDS data set and the construction of our source catalog and photometric database ([Section 2](#)). Next we describe the identification of likely late-type M dwarfs in this catalog and estimates of their physical properties ([Section 2.4](#)). We then present our method for identifying periodic variations in our photometric database and verify our ability to accurately recover rotation periods using these methods by constructing synthetic PS1-MDS light curves ([Section 3](#)). We then present the list of candidate rotating cool dwarfs ([Section 4](#)). Finally, in [Section 5](#), we discuss trends in our rotation period data set against stellar mass and X-ray luminosity in the context of recent results of contemporary studies. We additionally examine correlations between amplitude of variability for the final sample of rotating M dwarfs with respect to estimated stellar mass, as well as trends in amplitude of variability across the five PS1-MDS filters.

2. DATA PROCESSING

We sought to extract light curves for all of the cool stars in the PS1-MDS data set. To this end, we first constructed a catalog of star-like objects in the PS1-MDS deep co-adds ([Section 2.2](#)), then extracted photometry from the nightly stacks using this catalog as a reference ([Section 2.3](#)). We then investigated the light curves of the objects with colors consistent with cool stars ([Section 2.4](#)).

The goal in this work is to generate a small catalog of *high-confidence* cool stellar rotators, rather than a complete and/or statistically well-characterized sample. Our general strategy in the data processing was to set relatively loose limits on data quality in earlier stages of the pipeline, then excise bad data farther downstream,

culminating in the visual vetting of candidate rotators ([Section 3.2](#)).

2.1. Observations

The PS1-MDS was performed on the 1.8-meter PanSTARRS-1 telescope situated on Mount Haleakala, Hawai‘i, equipped with five broad-band filters, (*grizy*)_{P1}, and a 1.4-gigapixel detector composed of 60 edge-abutted 4800×4800 pixel CCDs with a pixel scale of 0.26 arcsec pixel⁻¹ ([Kaiser et al. 2010](#)). The PS1 filters are similar to those used in the Sloan Digital Sky Survey (SDSS) but include a *y*_{P1} filter ($\lambda_{\text{eff}} \sim 9600 \text{ \AA}$), a bluer cutoff in the *z* band ($\Delta\lambda \sim 1000 \text{ \AA}$ rather than 1400 \AA), a 200 \AA redder cutoff in the *g* band, and no *u* band ([Tonry et al. 2012](#)).

The Medium Deep Survey observed 10 fields spread out in right ascension over a span of five seasons. PS1-MDS observations were conducted nightly, rotating filters from one night to the next. Under normal conditions, *g*_{P1} and *r*_{P1} were observed on a single night, with *i*_{P1} following the next night and *z*_{P1} the night after, all to 5 σ depths of ~ 23.3 mag. PS1-MDS observed *y*_{P1} during bright periods with a 5 σ depth of ~ 21.7 mag. The future Large Synoptic Survey Telescope (LSST) data stream will resemble that of the PS1-MDS, but extend deeper (e.g., 5 σ single-visit depth of 24.7 in *r* band) and significantly wider (covering $\approx 3000 \text{ deg}^2$ per night; [Ivezić et al. 2008](#)).

Our analysis is based on data products from the “PV2” version of the PS1 data reduction. In this analysis the raw images are first processed by the Image Processing Pipeline (IPP), which applies standard calibrations and warps images onto a standard astrometric solution ([Magnier 2006](#)). As part of our studies of transients in the PS1-MDS data set, nightly and deep stacks of the IPP-processed PS1-MDS observations were downloaded to Harvard University’s *Odyssey* high-performance computing cluster and ingested into the *photpipe* pipeline originally developed for the SuperMACHO and ESSENCE projects ([Rest et al. 2005, 2014](#)). We conducted our study at a time when Pan-STARRS project resources were dedicated to the development of the “PV3” public data release and so we chose to derive our source catalogs and extract photometry using the resources available locally, namely the nightly and deep PV2 stack images. We did so using customized routines operating alongside the *photpipe* framework as described below. Future iterations of this project will leverage the final PV3 data products.

2.2. All-Source Catalog

We generated source catalogs by running SExtractor ([Bertin & Arnouts 1996](#)) on the *photpipe*-ingested *no-tyr1* stack images, which combine all observations ex-

cept for those obtained during the first year of PS1-MDS observations. Routines in `photpipe` normalize the SExtractor-reported fluxes onto the absolute photometric system defined by the `pv2e` ubercalibration of PS1 (D. Finkbeiner, 2016, priv. comm.; see also Finkbeiner et al. 2016). Because the stack images are of high quality, we used a low source detection threshold of 0.1σ above the sky level (SExtractor parameters `DETECT_THRESH` and `ANALYSIS_THRESH`), then flagged as dubious sources that had implausible SExtractor-reported parameters. In particular, we flagged sources that did not meet the following criteria:

- magnitude $2 < m < 28$ mag,
- magnitude error $dm < 0.4$ mag,
- no flag indicating nearby neighbors or bad pixels,
- no flag indicating that the object was deblended,
- major-axis FWHM $0 < fwhm1 < 25$ pixels,
- minor-axis FWHM $0 < fwhm2 < 185$ pixels,
- background level $900 < sky < 1200$ ($griz_{P1}$ images) or $2600 < sky < 4000$ (y_{P1}).

These cuts were determined empirically by examining the distributions of the parameters reported by SExtractor. The bimodality in the last criterion was needed because the y_{P1} band images are normalized to a different background level than images using the other filters. We further identified likely stellar sources using the following criteria:

- star/galaxy classifier `class` ≥ 0.9 ,
- elongation < 3 .

In practice, the constraint on elongation eliminated only a handful of candidate stellar sources in which SExtractor’s neural-network-based star-galaxy classifier misbehaved.

We constructed a final catalog of sources by merging the SExtractor source lists generated in the five filters with the list of photometric standards associated with the `pv2e` calibration data set, using a $0.3''$ positional match tolerance. We additionally flagged any sources that were detected in fewer than three of the five filters. The final source catalog contains 4,073,661 likely stellar sources not flagged by the above criteria. This may be compared to 342,762 objects in the `pv2e` catalog, which is limited to moderately bright sources with excellent photometric properties.

Table 1. Stellar locus slopes

Color-color plane	Slope
$(g-r-i)_{P1}$ ^a	0.403
$(r-i-z)_{P1}$	0.449
$(i-z-y)_{P1}$	0.417

^aThis locus transitions to be vertical at $(g-r, r-i)_{P1} = (1.23, 0.55)$ mag; see Figure 1.

2.3. Photometry

We extracted photometry from the nightly stacks using SExtractor in conjunction with PSFEx (Bertin 2011) to perform both PSF fitting and aperture photometry. Here SExtractor was run in “double-image” mode using the `notyr1` deep stacks to detect sources and the per-night images to measure their photometry; this strategy makes it possible to detect flares from stars that are seen in the deep stacks but generally too faint to be detected in the nightly stacks. We calibrated photometry for the individual epochs to the absolute scale by matching to the `pv2e` catalog and solving for a scale factor to apply to the measurements, $\log f_{\text{abs}} = \log_{\text{psf}} + m$. We used Markov Chain Monte Carlo (MCMC) sampling with `emcee` (Foreman-Mackey et al. 2013) to determine both the scale factor m and its uncertainty while accounting for the measurement uncertainties present in both catalogs. Epochs were rejected where the reduced χ^2 of the absolutization fit exceeded 2, the scale factor was negative, the fractional uncertainty in the scale factor exceeded 25%, or fewer than 10 sources were identified. (The typical 2960×2960 pixel² [740×740 arcsec²] image subsections that we analyze have $\sim 2,000$ sources, but many fewer can be present when the weather was poor or the subsection is on the very edge of the night’s sky coverage.) The final photometric data set consists of 443,747,494 measurements and upper limits across the five PS1-MDS filters, with ~ 41 million in g_{P1} , ~ 72 million in r_{P1} , ~ 149 million in i_{P1} , ~ 140 million in z_{P1} , and ~ 43 million in y_{P1} .

We obtained mean photometry for each of the cataloged sources by applying the same technique to the `notyr1` stacks. In these deeper images we found that we needed to add a fractional 3% photometric uncertainty in quadrature to the pipeline-reported values to ensure that the reduced χ^2 of the typical epoch stayed within the limit specified above. We also identified a handful of cases where the absolutization fit for the PSF fluxes required an additional term: $\log f_{\text{abs}} = k \log_{\text{psf}} + m$, where by default it was implicitly the case that $k = 1$. The me-

dian z_{P1} magnitude in our catalog is 23.31 mag, compared to 18.72 mag in pv2e.

2.4. Candidate Cool Dwarfs

We identified candidate cool dwarfs using color cuts as described below. Because the PS1 filters are not precisely the same as those used by SDSS, especially on the red end that is of greatest interest to us, we derived these cuts independently rather than reusing prior SDSS-based results (e.g., Kowalski et al. 2009), although alternatively PS1-SDSS color transformations could be applied (Tonry et al. 2012).

Figure 1 shows color-color diagrams for our flagged source catalog. In each such plane stellar sources are generally confined to a “stellar locus”, with the surrounding sources generally corresponding to galaxies (e.g., Morganson et al. 2015). We note that the reddening vector is fairly well-aligned with the stellar locus in the $(r-i-z)_{P1}$ and $(i-z-y)_{P1}$ planes (Green et al. 2015) and so reddening should not scatter many cool star candidates off the locus. We show below that for the stars that are bright enough for us to detect their periodic variability, reddening is generally a small effect.

For each color-color plane we determined the location of the stellar locus by binning the catalogued source colors into a 400×400 two-dimensional histogram, then fitting a slope to the positions of the 1600 most-populated bins. In the case of the $(g-r-i)_{P1}$ space, we modeled the locus as discontinuously transitioning to be vertical at $(g-r, r-i)_{P1} = (1.23, 0.55)$ mag as shown in Figure 1. This transition point marks the approximate beginning of the M dwarf sequence (e.g., Kraus & Hillenbrand 2007; Morganson et al. 2015). The parameters derived from these fits are reported in Table 1.

Figure 1 shows the results of the stellar locus color cut in each color-color space in addition to their intersection. As shown in the off-diagonal panels of Figure 1, the sources identified by a stellar locus color cut in any given color-color plane are subject to a large amount of scatter in the other two planes. The combination of the locus color cuts is therefore crucial in identifying the true stars in the sample. Although sources with upper limits consistent with the above criteria are included in the final sample, they are not shown in the figure.

We identified sources as potential cool stars if they were likely stellar sources (cf. Section 2.2) with mean catalog photometry meeting the following criteria:

- detections in the i_{P1} and z_{P1} bands,
- position consistent with the stellar locus,
- $(g-r)_{P1} > 1.0$ mag,
- $(r-i)_{P1} > 0.55$ mag, and

- $(i-z)_{P1} > 0.32$ mag.

The latter criteria roughly isolate stars of M spectral types and later. Here, based on inspection of color-color histograms, consistency with the stellar locus is defined as colors consistent with lying within 0.15 mag of our locus fits in all three color-color spaces. Sources near the vertical portion of the $(g-r-i)_{P1}$ locus had to lie within 0.10 mag of it. The total number of sources meeting these criteria was 184,148.

3. SEARCH FOR PERIODICITIES

We searched for periodic variations in the light curves of our candidate cool stars using the multiband extension of the Lomb-Scargle periodogram introduced by VanderPlas & Ivezić (2015). In this method, each source’s light curve is modeled as a combination of a “base” term, common to every filter, and “band” terms unique to each observed filter. Each term is expressed as a truncated Fourier series with N_{base} and N_{band} terms, respectively. This configuration yields two fundamental models, the “shared-phase” model ($N_{\text{base}} = 1$, $N_{\text{band}} = 0$) and the “multi-phase” model ($N_{\text{base}} = 0$, $N_{\text{band}} = 1$), as termed by VanderPlas & Ivezić (2015). For each candidate periodicity, the model is optimized in a least-squares sense using a Tikhonov regularization to push as much variation into the “base” term as the data allow.

In the case of starspots passing through the view of the observer, we expect the filters to share the same phase; we find that for the purposes of this study, the best results were achieved by computing periodograms with the shared-phase model after normalizing the light curves of each filter by dividing out their mean values. Though periods can still be recovered accurately without normalization, we choose to normalize the light curves because the amplitudes of unnormalized light curves tend to vary significantly from filter to filter. Our experience is consistent with various other studies in that extending past the simple sinusoidal model (i.e., $N_{\text{base}} > 1$) is not required for accurate period determination (see, e.g., Newton et al. 2016).

For each candidate cool star, we computed a periodogram using the gatspy implementation of the multiband periodogram provided by VanderPlas & Ivezić (2015), sampling 1000 periods logarithmically spaced between 0.7 and 300 days. We identified the best-fit period as the one resulting in the highest periodogram power, ignoring peaks between 0.9 and 1.1 days to avoid false signals associated with the observing cadence. We computed two significance metrics. R_s denotes the ratio between the powers of the best-fit and second-highest peaks in the periodogram, once again ignoring peaks around 1 day, while R_{80} refers to the ratio between the

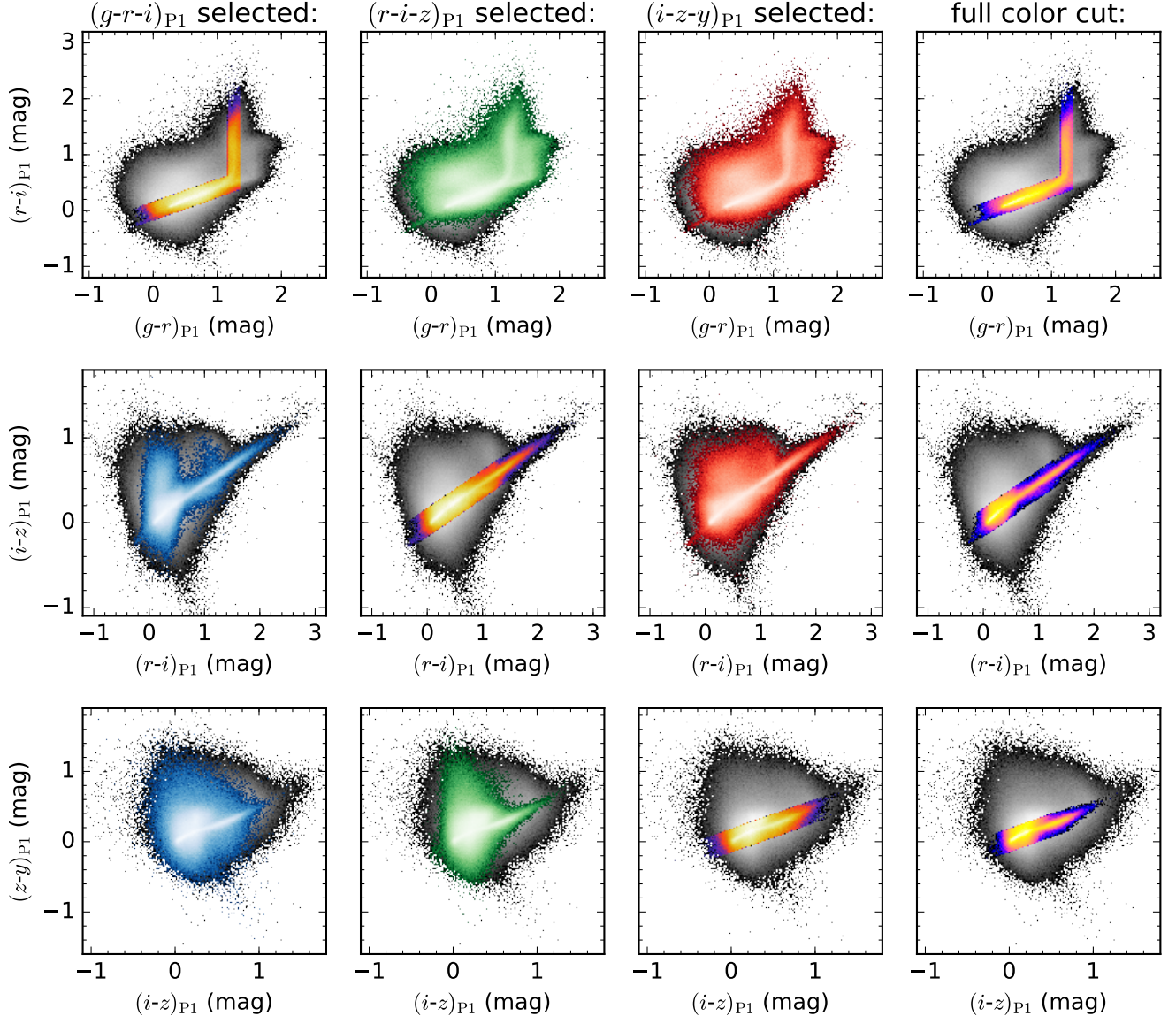


Figure 1. Color cuts applied to isolate the stellar locus in each color-color space. In each panel, the overall catalogued sample is shown in a grayscale 2D histogram, and selected sources are shown in color. In all cases the intensity scaling is logarithmic. *Leftmost column:* The results of the stellar locus cut in $(g-r-i)_{P1}$ plane. The top panel shows the distribution of sources that pass the $(g-r-i)_{P1}$ cut in the $(g-r-i)_{P1}$ color-color plane. The middle panel shows the $(g-r-i)_{P1}$ -selected sources in the $(r-i-z)_{P1}$ plane, and the lower panel shows them in the $(i-z-y)_{P1}$ plane. *Second column:* Similar to the leftmost column, but showing the results of the $(r-i-z)_{P1}$ cut in the three planes. *Third column:* Similar to the others, but showing the results of the $(i-z-y)_{P1}$ cut. *Rightmost column:* For each row, the result of the full color cut (the intersection of the $(g-r-i)_{P1}$, $(r-i-z)_{P1}$, and $(i-z-y)_{P1}$ individual color cuts) applied to $(g-r-i)_{P1}$, $(r-i-z)_{P1}$, and $(i-z-y)_{P1}$ color-color spaces, respectively.

power at the best-fit peak and the 80th percentile periodogram power. These parameters are illustrated in Figure 2. We use cuts on these significance parameters and visual vetting to identify rotating objects, which we describe below.

3.1. Synthetic Light Curves

To calibrate our significance cuts and test the robustness of the periodogram analysis, we computed periodograms for light curves with artificial periodicities,

injecting sinusoidal signals into the light curves of sources that had the lowest variability significance ratings ($R_s < 1.01$, where 1.0 is the lowest possible value of R_s). We drew quiescent light curves from across the survey at random in order to minimize the impact of location-dependent features of the light curves (due to, e.g. differences in the total number of observations). The injected signals had periods of 0.1–350 days and amplitudes of 1–5% that of the mean flux in each filter.

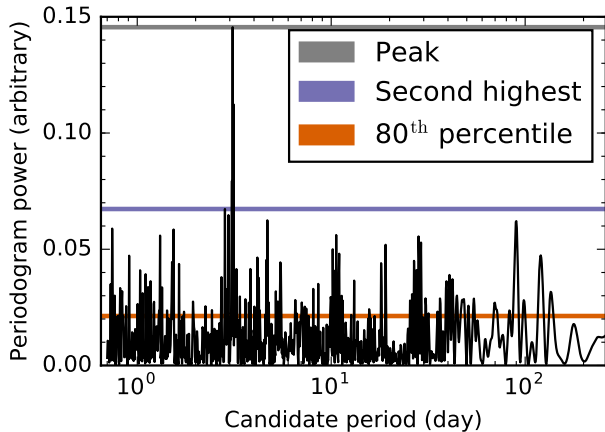


Figure 2. An example periodogram. R_s is calculated by dividing the power of the best-fit peak (shown in grey) and the power of the second-highest peak (shown in purple). R_{80} is calculated by dividing the power of the best-fit peak and the 80th percentile power value (shown in orange).

We set the range of injected periods outside the domain of the periodogram search (0.7–300 days) in order to investigate the behavior of the periodogram when the true rotation period is outside the range of possible periods.

We generated a set of 30,884 synthetic lightcurves using quiescent sources with $17.0 < z_{P1} < 18.0$ mag. This range was chosen based upon the apparent magnitudes of the rotating M dwarfs in our final sample. The overall rate of successful recoveries was 79.5%, where we define a successful recovery as one in which the the strongest periodogram peak met our significance cuts (see below) and the periodogram-derived period matched the injected period to within 30%. For 9.5% of sources, an accurate period (again, where the derived and injected periods matched to within 30%) was recovered, but the periodogram did not pass our significance cuts. We generated an additional set of synthetic light curves from sources with $z_{P1} < 22$ mag in order to test recovery rates for the dataset as a whole. In the $z_{P1} < 22$ mag sample, the successful recovery rate was 73.8%. 12.2% of sources in this sample had accurate periods with periodograms that did not pass our significance cuts.

The leftmost panel of [Figure 3](#) plots the injected period versus the recovered period in the bright sample of synthetic light curves, while the middle panel shows the same for the union of the two synthetic samples. Although aliased periods are visible along curved tracks about the 1:1 line in both panels, the aliased periods (and other incorrectly recovered periods) are significantly more prominent in the full data set. Beat frequencies between the true period and one-day observing cadence can also be seen at small periods, as shown in the rightmost panel of [Figure 3](#).

[Figure 4](#) shows the recovery fraction as a function of

injected period and amplitude of variability for the full synthetic data set. A drop in the recovery fraction between 2 and 10 days is visible, which we attribute to the beat frequencies shown at right in [Figure 3](#). The periodogram shows a moderate increase in performance with increasing period at amplitudes above 2.0%. At amplitudes below 2.0%, there is no strong increase in recovery fraction with period.

We additionally tested our ability to recover periodic signals faster than the daily observation cadence. We generated a sample of 4112 synthetic light curves with injected periods ranging from 0.1 to 1.0 days. The shortest injected period that was successfully recovered was 0.613 days. For periods between 0.613 and 1.0 days, the successful recovery rate was 36%, significantly lower than the recovery rate for periods above 1 day. However, of the 1307 sources with a recovered period of <1.0 day, 72.5% of sources had an injected period of <1.0 day.

Table 2. Successful and unsuccessful recoveries in synthetic data

Cut type	Successes : failures
$R_{80} > 10.5$	38119 : 2548
$R_s > 2.3$	6211 : 196
$R_{80} > 10.5$ and $R_s > 2.3$	6074 : 176
$R_{80} > 10.5$ or $R_s > 2.3$	38256 : 2568

3.2. Significance Cuts and Visual Vetting

We chose a subsample of periodograms to vet visually using significance cuts on the R_{80} and R_s metrics. [Figure 5](#) shows the distributions these values in the synthetic sample. We examined all periodograms having $R_{80} > 10.5$ or $R_s > 2.3$, as shown by the green lines. While R_s is not a useful significance metric for periods above ~ 10 days, we included it in the significance cut because there are 137 synthetic rapid rotators that pass the R_s cut but not the R_{80} cut. The overall numbers of successful and unsuccessful recoveries yielded by these cuts in the full synthetic data set are presented in [Table 2](#).

Concerning rapid rotators, 558 sources with an injected period of less than 1.0 day had a strongest periodogram peak located at $P \leq 1$ day that passed our significance cuts. Conversely, 117 sources with an injected period of more than 1.0 day were classified as rotators with a period of less than 1.0 day. We therefore conclude that the periodogram is able to identify sources with rotation periods faster than the cadence of observation, but does not constrain their periods well.

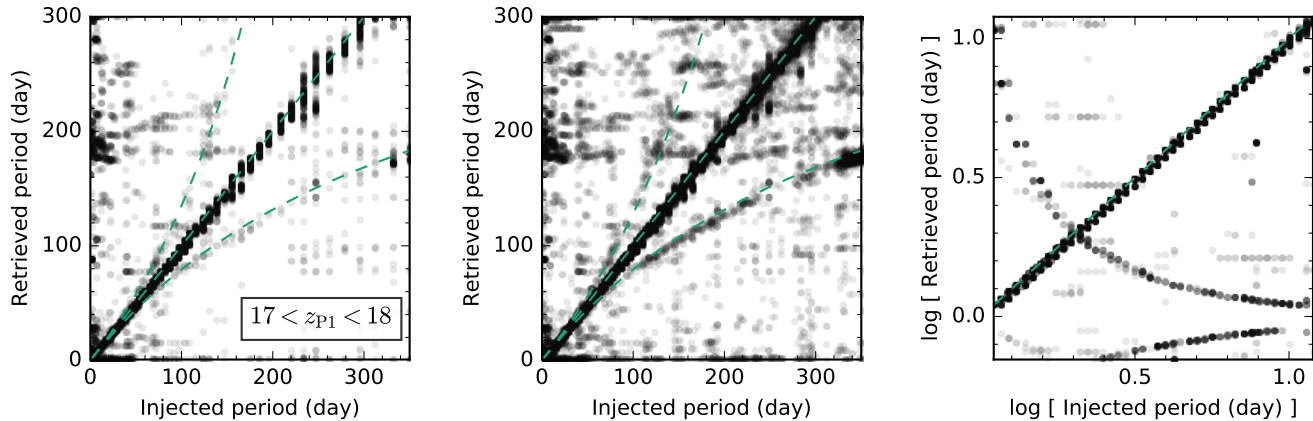


Figure 3. Input period versus output period for the synthetic light curves. *Left panel:* Input period versus output period for those sources with $17 < z_{P1} < 18$. *Middle panel:* The same, for all sources in the synthetic catalog ($z_{P1} < 22$). *Right panel:* A log-scale zoom in of the middle panel for injected periods between 0.7 and 20 days. Beat frequencies with the one day observing cadence are clearly visible along the curved tracks, as shown by the dashed green lines.

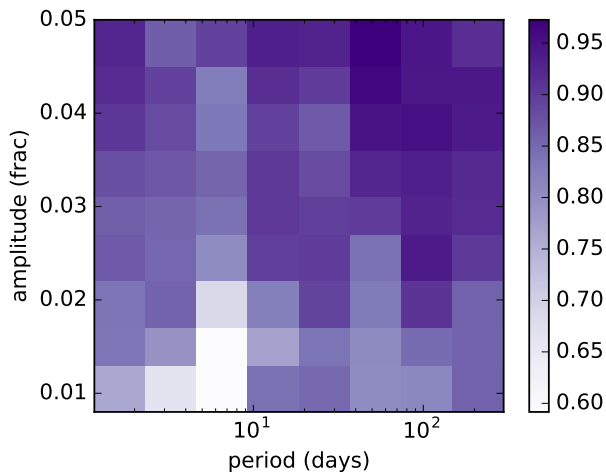


Figure 4. Period recovery fraction as a function of injected period (x-axis) and amplitude (y-axis). Synthetic light curves with a low amplitude of variability and short period are recovered relatively less often than the bulk of the synthetic sample. We attribute the low success rate at $3 \lesssim (P_{\text{rot}}/\text{day}) \lesssim 10$ and small amplitudes to the effect of aliases with with observing cadence and harmonics (Figure 3, rightmost panel). Injected periods outside the recovery range (i.e. $P_{\text{rot}} > 300$ days) are excluded from this figure. Each bin contains between 215 and 680 contributing sources, with a median of 480 contributing sources.

In the full sample of candidate cool stars, 1,067 sources met the significance criteria. Two authors (EKF and PKGW) then separately performed a visual vetting of these sources’ light curves, periodograms, and SEDs. Of the 1,067 candidates, both vetters independently agreed that 271 of them were secure detections of rotation.

The uncertainty in the measured rotation period increases with increasing period, given that fewer periods are observed with the time frame of the survey. To estimate this uncertainty, we ran the multiband Lomb-

Scargle periodogram on the final sample of rotators with a more finely spaced array of trial rotation periods, and measure the width of the primary peak of the periodogram. We caution, however, that the sources with $P_{\text{rot}} < 1.0$ days are subject to greater uncertainty than the value derived in this way, for the reasons described above.

4. A CATALOG OF PS1 ROTATING COOL DWARFS

We list the confirmed rotators in Table 3. A sample of phased light curves with periods spanning 0.72–112.4 days is shown in Figure 6. We examined image cutouts of these sources in the MDS deep stacks, 2MASS Atlas images (Skrutskie et al. 2006), and the “unWISE” unblurred WISE coadds including NEOWISE-Reactivation data (Lang 2014; Meisner et al. 2016). Nearly all (265) of the confirmed rotators are securely detected in the AllWISE source catalog (Cutri et al. 2013), and we use these identifiers whenever possible. Five additional sources are detected in the Sloan Digital Sky Survey Data Release 9 catalog (Ahn et al. 2012). Fewer sources are detected in 2MASS (230) than either of these surveys. One source is not found in any of the standard all-sky catalogs we have consulted, and we name it PSO J053.3285–27.1683; it lies outside the SDSS footprint. In every case, the sources without corresponding AllWISE catalog entries are perceptible in the unWISE coadds, but are blended with brighter neighbors due to the telescope’s relatively poor 6” resolution. This suggests that improvements in the AllWISE source extraction pipeline could lead to their recovery and measurement of their WISE photometry.

Table 3 includes dereddened z_{P1} magnitudes (see below) and $(grizy)_{P1}$ colors derived from the notyr1 stack images, placed onto the ubercalibrated pv2e absolute

Table 3. Candidate Rotating M Dwarfs^a

Name	z_{P1} (mag)	$(g-r)_{P1}$ (mag)	$(r-i)_{P1}$ (mag)	$(i-z)_{P1}$ (mag)	$(z-y)_{P1}$ (mag)	T_{eff} (K)	Mass (M_{\odot})	d (pc)	$\log_{10} L_{\text{bol}}$ [L_{\odot}]	Giant?	P_{rot} (day)	Ampl. (%)	Pk. Rat.	R_{80}
(1)	(2)	(3)	(4)	(5)	(6)	(7)	(8)	(9)	(10)	(11)	(12)	(13)	(14)	(15)
WISEA J021823.69-044932.5	17.72 ± 0.03	1.29 ± 0.05	1.65 ± 0.05	0.75 ± 0.05	0.39 ± 0.05	3130 ± 80	0.21 ± 0.04	350 ± 70	-2.3 ± 0.2		13.37 ± 0.03	2.1	1.71	12
WISEA J021907.51-033114.2	16.74 ± 0.03	1.32 ± 0.05	1.77 ± 0.05	0.80 ± 0.05	0.41 ± 0.05	3060 ± 80	0.17 ± 0.03	190 ± 40	-2.4 ± 0.2		12.39 ± 0.03	4.0	2.30	38
WISEA J022042.16-030701.0	16.38 ± 0.03	1.22 ± 0.05	1.10 ± 0.05	0.52 ± 0.05	0.23 ± 0.05	3470 ± 80	0.40 ± 0.07	390 ± 80	-1.7 ± 0.2		2.195 ± 0.003	2.1	1.37	26
WISEA J022049.11-041237.1	19.41 ± 0.03	1.20 ± 0.06	1.66 ± 0.05	0.76 ± 0.05	0.38 ± 0.05	3160 ± 80	0.24 ± 0.04	740 ± 100	-2.3 ± 0.2	?	25.57 ± 0.10	3.9	1.84	22
WISEA J022106.66-033528.4	17.72 ± 0.03	1.27 ± 0.05	1.45 ± 0.05	0.65 ± 0.05	0.30 ± 0.05	3260 ± 80	0.28 ± 0.05	480 ± 90	-2.0 ± 0.2	?	16.48 ± 0.05	4.4	1.91	41
WISEA J022113.86-052801.8	18.31 ± 0.03	1.34 ± 0.05	1.76 ± 0.05	0.83 ± 0.05	0.37 ± 0.05	3030 ± 80	0.16 ± 0.03	360 ± 70	-2.5 ± 0.2	?	1.6248 ± 0.0006	1.9	2.91	12
WISEA J022121.80-043127.9	16.58 ± 0.03	1.27 ± 0.05	1.44 ± 0.05	0.66 ± 0.05	0.30 ± 0.04	3240 ± 80	0.27 ± 0.05	280 ± 50	-2.0 ± 0.2		1.3370 ± 0.0003	1.2	1.23	20
WISEA J022253.37-043254.3	16.87 ± 0.03	1.21 ± 0.05	0.84 ± 0.05	0.39 ± 0.05	0.19 ± 0.05	3700 ± 80	0.53 ± 0.10	720 ± 100	-1.3 ± 0.2		5.203 ± 0.004	2.8	5.59	25
WISEA J022325.43-052529.4	17.03 ± 0.03	1.07 ± 0.05	0.68 ± 0.05	0.34 ± 0.05	0.20 ± 0.05	3890 ± 80	0.69 ± 0.10	900 ± 200	-1.2 ± 0.2	P	36.2 ± 0.3	5.2	1.93	19
WISEA J022327.16-052055.0	15.85 ± 0.03	1.22 ± 0.05	1.42 ± 0.05	0.65 ± 0.05	0.30 ± 0.05	3290 ± 80	0.30 ± 0.05	200 ± 40	-2.0 ± 0.2		4.019 ± 0.003	1.9	4.10	12
WISEA J022400.58-052005.1	16.36 ± 0.03	1.15 ± 0.05	1.40 ± 0.05	0.62 ± 0.05	0.31 ± 0.05	3370 ± 80	0.37 ± 0.07	280 ± 60	-1.9 ± 0.2		60.9 ± 0.5	1.6	1.08	11
WISEA J022411.77-041527.7	17.86 ± 0.03			0.74 ± 0.05	0.27 ± 0.05	3170 ± 90	0.23 ± 0.04	380 ± 80	-2.3 ± 0.2	?	1.3451 ± 0.0010	4.1	1.22	28

NOTE—Missing values in columns (3) through (6) may occur if the deep photometric extraction failed due to missing data or an inability to determine the absolute photometric calibration. Columns (7) through (10) are estimated from colors as described in Appendix A. A “p” in column (11) indicates a probable giant; a “?” indicates a source missing the robust 2MASS and/or WISE photometry needed to assess the criterion. Column (13) is the semi-amplitude of the periodic variability signal. Columns (14) and (15) are the periodogram significance metrics discussed in Section 3.

^a This is a sample version of this table showing only the first few rows. The full table is available in machine-readable form.

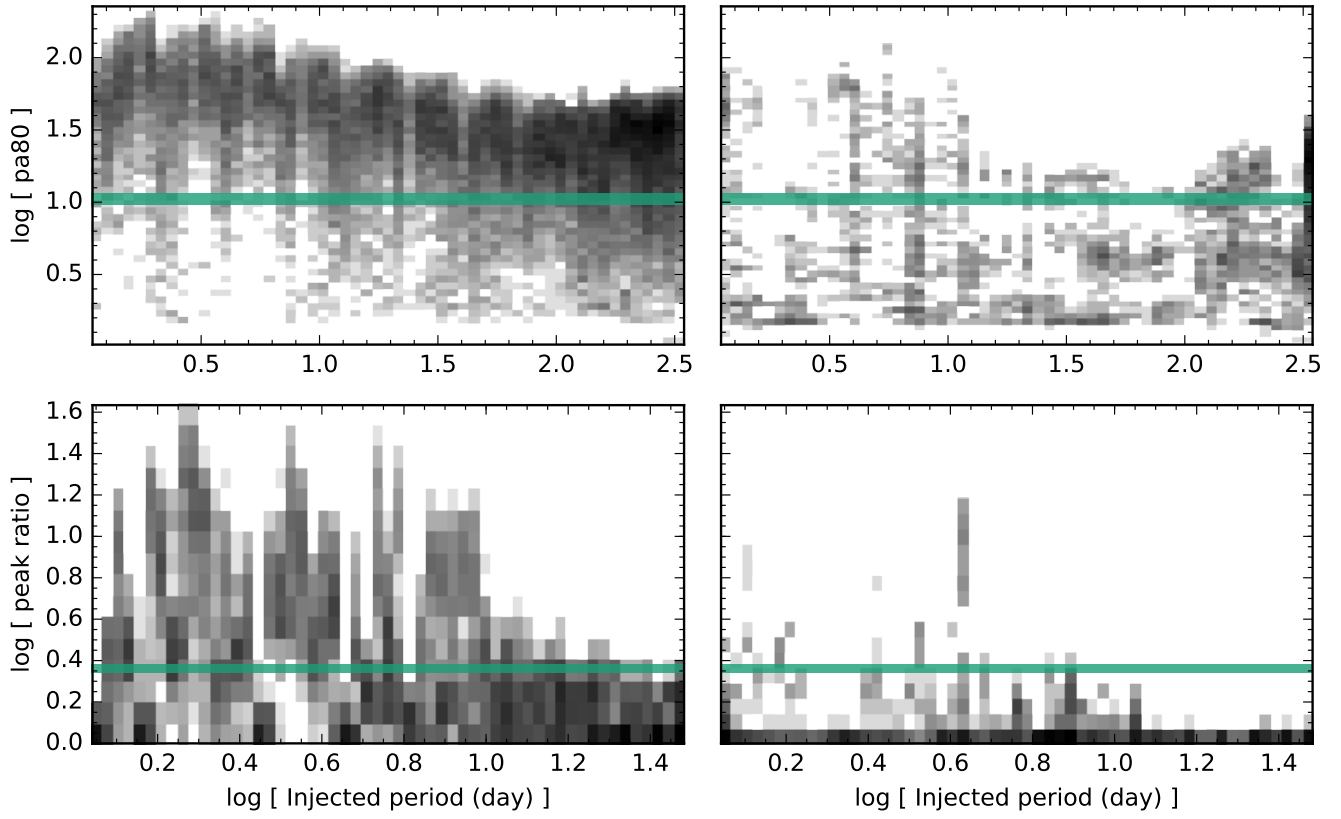


Figure 5. *Left column:* The distribution of input period versus R_{80} (*top row*) and R_s (*bottom row*) for those sources in which the recovered period is within 30% of the true period. *Right column:* The same for those sources in which the recovered period is not within 30% of the true period. The green horizontal lines show the cutoffs used to select sources for visual vetting.

photometric system as described in Section 2. We additionally report estimated effective temperatures, masses, distances, and bolometric luminosities computed as described below. While our effective temperature measurements are believed to be fairly accurate ($\sim 3\%$), the other quantities are difficult to determine from colors alone and are uncertain at the $\sim 20\%$ level. Finally, we report the key parameters determined from our periodicity search (Section 3).

4.1. Estimated Stellar Properties

We estimated the physical properties of the vetted rotators from their colors and apparent magnitudes. We describe the full procedure in Appendix A but also summarize it here. First, using the filter bandpasses provided by Tonry et al. (2012) and the flux-calibrated spectra and fundamental parameters of the M dwarf sample developed by Mann et al. (2015, 2016), we computed new polynomial relations between PS1 colors and several stellar parameters: mass (M), effective temperature (T_{eff}), absolute z_{P1} magnitude ($M_{z,\text{P1}}$), and the z_{P1} -band bolometric correction factor ($\text{BC}_{z,\text{P1}}$). Appendix A includes tables of the polynomial coefficients for use in future PS1 studies of cool stars.

We then simultaneously estimated the distance and reddening of each star, combining our $M_{z,\text{P1}}$ relation with the three-dimensional PS1 dust maps of Green et al. (2015). In the final catalog the median A_V is 0.04 mag, the 95th percentile is 0.22 mag, and the typical distance uncertainty is 20%.

Finally, we used our polynomial relations and dereddened colors to estimate T_{eff} , M , and the bolometric flux f_{bol} for each rotator. A detailed description of the derivations of each of these parameters may be found in Mann et al. (2015, 2016). Based on the scatter in our polynomial fits and the T_{eff} calibration standards used by Mann et al. (2015, 2016), the uncertainties in our T_{eff} values are 80 K, or $\lesssim 3\%$, and those on f_{bol} are $\sim 4\%$. The uncertainties in M , on the other hand, are $\sim 20\%$.

4.2. Cross-Identifications

We cross-matched our catalog against the SDSS DR9 catalog (Ahn et al. 2012), the AllWISE catalog (Cutri et al. 2013), the 2MASS Point Source Catalog (Skrutskie et al. 2006), the UKIDSS Large Area Survey catalog (Lawrence et al. 2007), and the third (2005 September) release of the Deep Near-IR Survey of the Southern Sky (DENIS; Vauglin et al. 1999) using the VizieR web service (Ochsenbein et al. 2000) through the astroquery Python module¹. Table 4 summarizes the results of the cross-matches and stands in for a machine-readable ta-

ble (MRT) provided with this article that includes the cross-matched identifiers and basic photometric measurements in the 19 additional filters provided by these surveys.

Table 4. Summary of MRT of optical/IR cross-matches^a

Survey	Number of matches	Photometric filters
This work	271 ^b	(<i>grizy</i>) _{P1}
SDSS	249	<i>u g r i z</i>
AllWISE	265	W1 W2 W3 W4
2MASS	230	J H K _s
ULAS	81	Y J H K
DENIS	64	I J K

^a This table summarizes the contents of a machine-readable table containing cross-matched optical/IR identifiers and photometry.

^b For convenience, the MRT duplicates the (*grizy*)_{P1} photometry presented in Table 3.

We also cross-matched our catalog with a variety of X-ray surveys. After manual inspection of the cross-match results, we identified X-ray counterparts for 22 sources. The X-ray properties of these sources are summarized in Table 5. We have preferred measurements from the *Chandra* Source Catalog (CSC) version 1.1 (Evans et al. 2010) when available (eight sources). Eleven additional sources have matches in the 3XMM-DR5 catalog (Rosen et al. 2016), and the final three sources are found in the XMM-LSS catalog (Chiappetti et al. 2013). In Table 5 we have converted X-ray fluxes to a common energy band of 0.2–2 keV as in Cook et al. (2014) from the energy ranges used in the catalogs: 0.5–7 keV for CSC 1.1; 0.5–4.5 keV for 3XMM-DR5; and 0.5–2 keV for XMM-LSS. Using PIMMS and an APEC model to determine the conversion factors, we multiplied the catalog fluxes by 1.21, 1.21, and 1.26, respectively (see Cook et al. 2014 for details).

4.3. Contaminants

Our optically-based selection of cool stars could result in contamination of the sample by M giants. Lacking spectroscopic follow-up, some insight into the contamination can be gained by considering infrared colors (Bessell & Brett 1988; Li et al. 2016). For those of our sources with robust cross-matches to both the 2MASS and WISE catalogs, we have tested the criterion given in Equation 1 of Li et al. (2016), which categorizes probable M giants based on their position in the $W1-W2/J-K$ color space. Here we did not attempt to deredden the catalogued 2MASS and WISE magnitudes. We find three sources that are classified as probable giants by the criterion: WISEA J022325.43–052529.4 ($P_{\text{rot}} = 36.2 \pm 0.3$ d), WISEA J095821.50+030242.6 ($P_{\text{rot}} = 16.30 \pm$

¹ <http://www.astropy.org/astroquery/>

0.05 d), and WISEA J221306.75–001313.0 ($P_{\text{rot}} = 30.8 \pm 0.2$ d). While 101 sources lack sufficient information to evaluate the criterion, examination of our catalog in other color spaces such as $(g-i)_{\text{P1}}/J-K$ (Brown et al. 2011) does not yield any likely examples of additional giant contaminants. Table 3 flags the three objects selected as probable giants. They are not included in subsequent analysis.

By construction, any spatially unresolved binaries in our catalog must have $(g-r-i-z-y)_{\text{P1}}$ colors consistent with single M stars. Since the hotter star in such a pair dominates the radiative output, such systems likely contain two low-mass stars and should not be considered “contaminants” *per se*. However, our estimates of mass and other stellar parameters will be inaccurate in such systems. Lacking spectroscopic follow-up or precise distance estimates, we are unable to identify probable binaries in the current data set. Covey et al. (2016) identified a sample of 132 young, low-mass ($M < 0.5 M_{\odot}$) stars with photometric rotation periods in the Pleiades. Leveraging the fact that their targets all lie at approximately the same distance, they identified 20 of these sources as likely binaries from their position on a $V-K$ color-magnitude diagram. If the multiplicity in this cluster is approximately the same as that in the field, this suggests that $\sim 15\%$ of our sources are unresolved binaries

5. DISCUSSION

5.1. Characteristics of the Rotating Sample

Figure 7 visually summarizes the characteristics of the stars with rotation periods detected in our study. The $(i-z)_{\text{P1}}$ colors of the bulk of the stars range from ~ 0.3 – 1.1 mag, corresponding to a mass range of ~ 0.7 – $0.09 M_{\odot}$ and a T_{eff} range of ~ 3900 – 2800 K in our adopted models. Two unusually red sources have $(i-z)_{\text{P1}} = 1.14$ (WISEA J160316.52+541556.7, $P_{\text{rot}} \sim 100$ d) and $(i-z)_{\text{P1}} = 1.38$ (WISEA J221445.29+004500.7, $P_{\text{rot}} \sim 2$ d). The detected rotation periods range between ~ 1 – 130 d, with an approximately uniform distribution in $\log P_{\text{rot}}$. Although our tests with synthetic PS1-MDS light curves indicate that we should be sensitive to extremely slow ($P_{\text{rot}} > 150$ d) rotators, we do not find such a population in the present sample. However, it is important to note that the sample at hand includes only the most secure period measurements of the dataset — 40 out of 1067 of the sources in the automated sample did have $P_{\text{rot}} > 150$, but were removed from the final sample during visual vetting. We therefore cannot exclude the possibility that there exist very slow rotators in the data that were ruled as marginal detections during the construction of the present sample. The median estimated distance is 440 pc, with the redder (and

therefore intrinsically fainter) objects estimated to be nearer. The object with the smallest estimated distance is WISEA J141327.57+524831.6 ($P_{\text{rot}} \sim 0.8$ d), at ~ 90 pc.

The top two panels of Figure 7 suggest that our search has fairly uniform sensitivity across a range of $(i-z)_{\text{P1}}$ colors, apparent z_{P1} magnitudes, and rotation periods. As the bottom panel of Figure 7 demonstrates, however, several important biases are at work in the construction of our catalog. Our sample is derived from flux-limited catalogs and spans a wide range in T_{eff} , inducing color-dependent trends. We are only sensitive to objects with rotation periods $\gtrsim 0.7$ d and variability semi-amplitudes $\gtrsim 1\%$, while a search for periodic variability in the more photometrically stable *Kepler* data set suggests that the bulk of periodically variable objects have lower amplitudes (McQuillan et al. 2014), although that data set is dominated by stars hotter than those in our sample. Finally, we are not able to distinguish multiple systems from single stars in our catalog.

Figure 8 compares our sample to those presented in several comparable studies (McQuillan et al. 2013, 2014; Newton et al. 2016). One version of the plot differentiates stars based on each study’s estimated stellar masses. However, our masses have $\sim 20\%$ uncertainties, and the masses tabulated by McQuillan et al. (2013, 2014) are those provided in the Kepler Input Catalog (KIC; Brown et al. 2011), which are known to be systematically biased at low masses (Dressing & Charbonneau 2013). We therefore also use MEarth – K_s or pseudoMEarth – K_s color as the abscissa, where the utility of this quantity is discussed by Dittmann et al. (2016) and the pseudo-MEarth magnitude is defined by Newton et al. (2016):

$$\text{pseudoMEarth} = (i_{\text{SDSS}} + 2z_{\text{SDSS}})/3 - 0.20 \text{ mag.} \quad (1)$$

The scatter in the relation is asserted to be $\sim 5\%$. In this version of the plot we could only include the 211 sources for which we found both SDSS and 2MASS cross-matches. Using the Tonry et al. (2012) relations to synthesize SDSS magnitudes adds another 19 sources but does not change the fundamental character of the plot.

Figure 8 must be interpreted with care because each study is subject to different selection biases. For instance, it is clear that our study is less sensitive to fast rotators than the others, which is to be expected since the other studies are based on data taken more frequently than our daily cadence. We reiterate that the rotators in our sample with periods lower than the daily cadence should be considered to be significantly more uncertain than measurements of longer periods. We are also not sensitive to low-amplitude rotators. These are responsible for the dense stripes at relatively long ro-

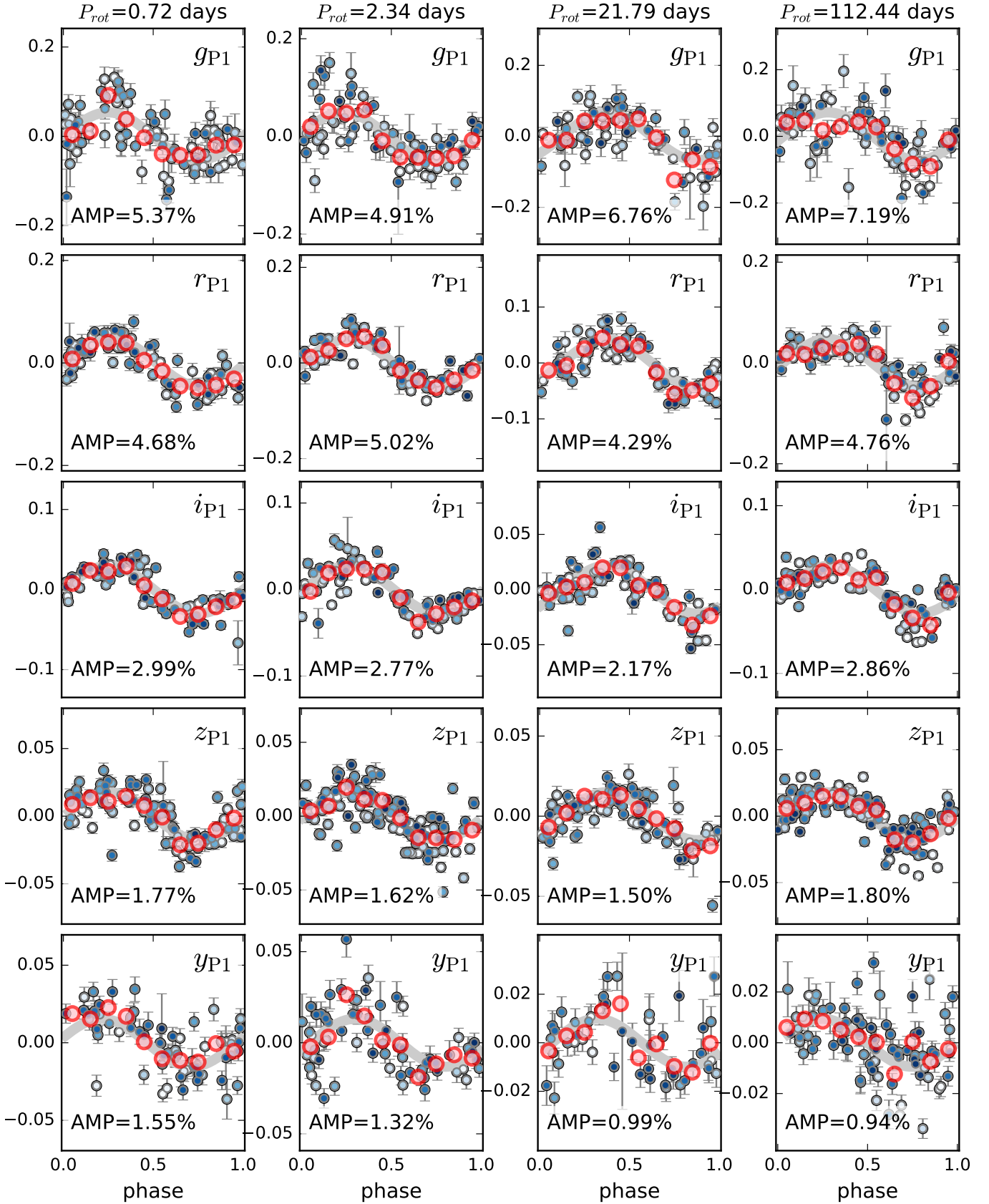


Figure 6. Phased light curves drawn from the final sample of rotating M dwarfs, with periods spanning 0.7 to 113 days. The red points show the phased light curve of the source, colored by time of observation, the purple points show the binned mean flux, and the model of the light curve for each filter is shown by the gray curve. The amplitude of variability estimated from the model of the source light curve is tabulated in the bottom left corner of each panel. From left to right, the sources plotted are: WISEA J104946.22+573026.7, WISEA J084921.27+444949.2, WISEA J100031.55+032820.9, and WISEA J083701.66+441542.6.

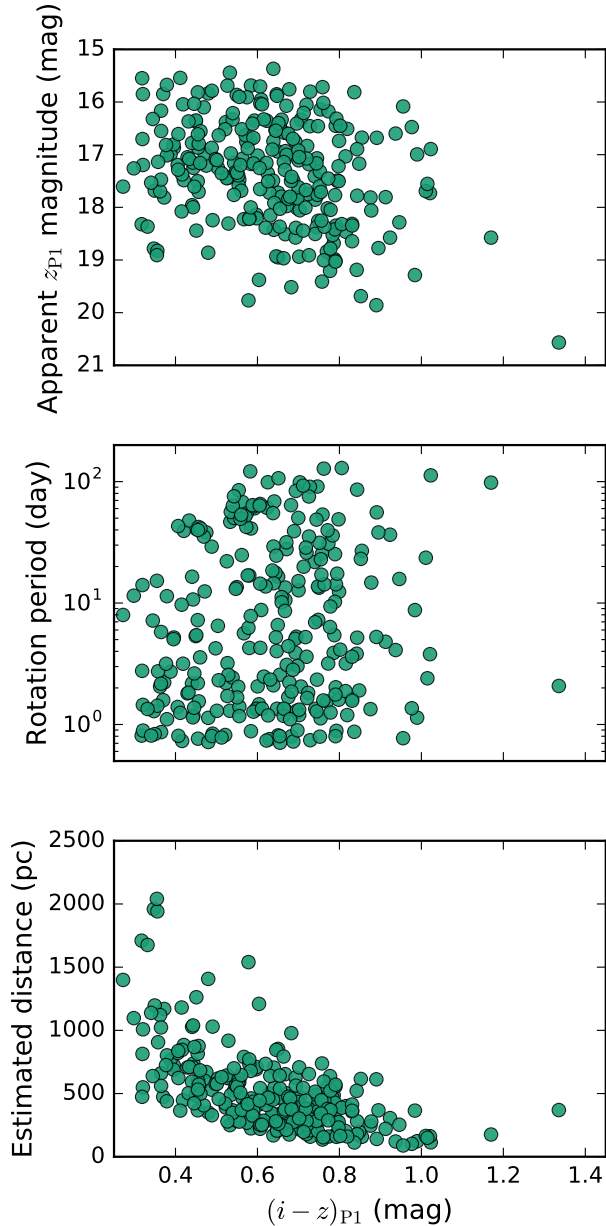


Figure 7. Observed and derived properties of our sample of 271 rotating cool stars. From top to bottom: apparent z_{P1} magnitude, rotation period, and estimated distance (Appendix A).

tation periods in the *Kepler* sample (McQuillan et al. 2014, their Figure 4), which explains why our sample does not show an analogous feature in Figure 8. We defer a full comparison of the data sets shown in Figure 8 to future work but consider a few points below.

5.2. Very Slow Rotators

In terms of either modeled stellar mass or (pseudo)MEarth $-K_s$ color, our sample bridges the *Kepler*-based data set of McQuillan et al. (2013, 2014),

which generally targeted stars with $M \gtrsim 0.35 M_{\odot}$, and studies of nearby, bright M dwarfs (Irwin et al. 2011; Newton et al. 2016) using the MEarth data set, which targeted stars below this threshold. This is useful because it helps differentiate trends that may be due to systematic effects from ones that are more likely to be astrophysical. For instance, Newton et al. (2016) noted that the MEarth data set contains a substantial number of objects with rotation periods > 70 d, while McQuillan et al. (2013, 2014) found none in *Kepler*. They suggested that this may lack may have been due to *Kepler* systematics, especially the effects of the quarterly reorientation of the spacecraft. We find tentative evidence that this is the case, because our much smaller sample recovers two objects with $P_{\text{rot}} > 70$ d, WISEA J141100.79+541430.7 and WISEA J232843.05+004453.1, at pseudoMEarth $-K_s < 2.2$ mag, a regime in which *Kepler* had good coverage. Analogous objects should exist in the *Kepler* data set, and the lack of any detections suggests that searches to date have not been sensitive to them. With only two such examples, however, firm conclusions cannot yet be drawn. Based on our data alone, it is possible that only stars with (pseudo)MEarth $-K_s \gtrsim 2.0$ mag or $M \lesssim 0.45 M_{\odot}$ are very slow rotators, but we have very few stars with (pseudo)MEarth $-K_s < 2.0$ mag, and our mass estimates are imprecise. It is also possible that very slowly-rotating stars exist on the blue / high-mass sides of these thresholds, but that such stars do not possess the nonaxisymmetric photospheric inhomogeneities that make them discoverable in photometric rotation period searches.

5.3. Amplitude of Variability

Figure 9 shows the relationship between rotation period and variability semi-amplitude in our final sample. We emulate Newton et al. (2016) by partitioning our targets into those with estimated masses larger or smaller than $0.25 M_{\odot}$. While the semi-amplitudes we find are larger than those of Newton et al. (2016), the shapes of the distributions we find are largely similar, with a marked lack of high-amplitude slow rotators. A notable exception is that we observe hints of an anti-correlation between rotation period and semi-amplitude in both mass bins, while Newton et al. (2016) do not see one in the lower-mass objects. Unlike Newton et al. (2016), however, we have not isolated a “statistical sample” that attempts to account for sensitivity effects and multiplicity, and high-amplitude and/or short-period objects will be overrepresented in our sample compared to their true prevalence due to their relative ease of detection.

Our sample, like that of Newton et al. (2016), shows a dearth of low-mass M dwarfs with intermediate rotation periods and low variability amplitudes. The larger samples of McQuillan et al. (2013, 2014) and Newton et al.

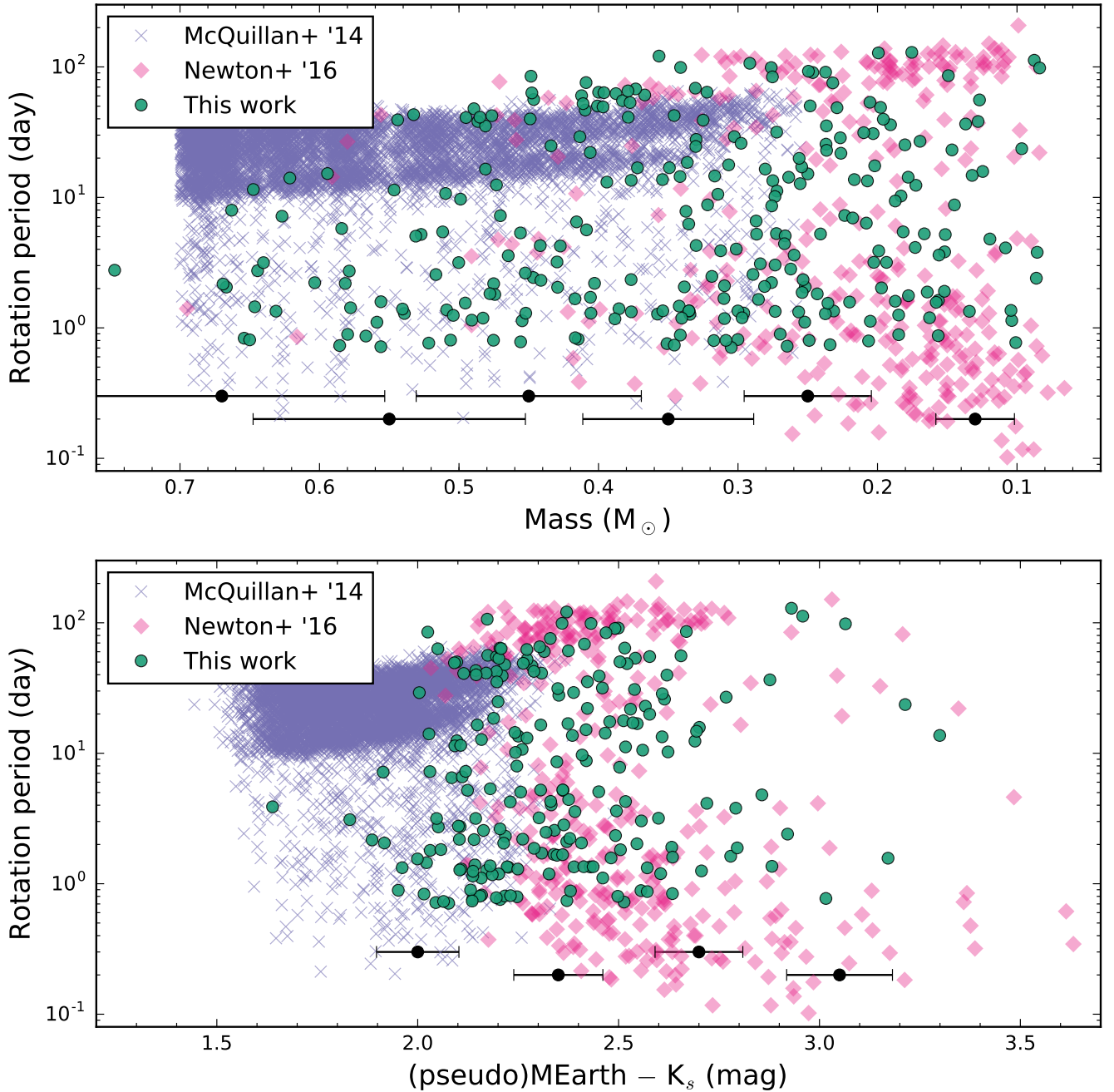


Figure 8. Three samples of stars with photometric rotation measurements. *Purple x's*: $\sim 6,200$ stars from an overall sample of $\sim 34,000$ found in the *Kepler* data set (McQuillan et al. 2013, 2014). *Pink diamonds*: 428 stars found in the M_{Earth} data set (Newton et al. 2016). *Green circles*: 271 stars found in this work. *Black errorbars* show typical uncertainties in the abscissa values for our data. *Upper panel*: the full sample, using estimated stellar masses as the abscissa. Each study estimates masses using a different method, and the estimates used by McQuillan et al. (2013, 2014) are known to be biased (Dressing & Charbonneau 2013). *Lower panel*: a reduced sample using (pseudo)M_{Earth} - K_s as the abscissa, discarding non-M_{Earth} sources without 2MASS cross-matches (see Section 5 and Dittmann et al. 2016). Our sample bridges the mass/color ranges best probed by *Kepler* and M_{Earth}. We emphasize that each study is subject to different selection effects, so intercomparisons should be performed with care.

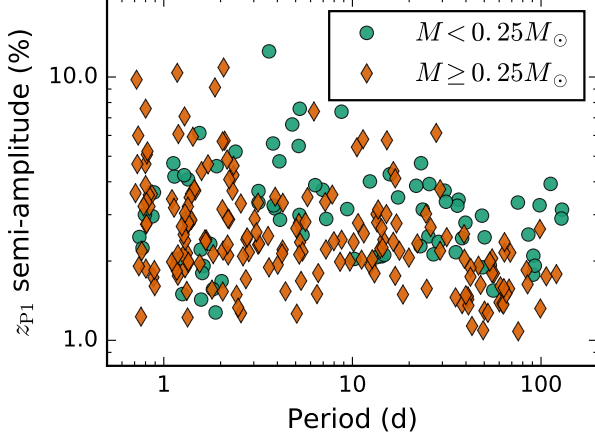


Figure 9. Variability amplitude in the z_{P1} band as a function of rotation period. The gap in periods at 0.9–1.1 days comes from cuts to avoid false detections near the daily observing cadence of PS1-MDS. There is an underdensity of low-mass sources at semi-amplitudes $\lesssim 2\%$ in the period range 3–40 d despite the fact that our search is not unusually insensitive to these sources (Figure 4).

(2016) have provided compelling evidence that there is a genuine overall lack of low-mass dwarfs at intermediate rotation periods, reminiscent of studies of magnetic activity (e.g., Gizis et al. 2002; Browning et al. 2010) tracing back to the “gap” in Ca II H&K emission in F and G stars discovered by Vaughan & Preston (1980). Newton et al. (2016) suggest that this gap exists because low-mass M dwarfs suddenly undergo rapid spin-down at intermediate ages. If this hypothesis is correct, this spin-down is apparently associated with high levels of non-axisymmetric photospheric inhomogeneity. An analogous gap in rotation periods has been observed in young clusters (e.g., Meibom et al. 2011) and is possibly explained by a rapid simplification of the magnetic field topology that leads to a large increase in angular momentum loss rates (Garraffo et al. 2015). Such a transition could plausibly lead to large, stable magnetic spots, consistent with the high-amplitude variability seen here.

5.4. Wavelength-Dependence of Variability Amplitude

Unlike other large surveys for stellar rotational modulation, our study includes data in five photometric filters, allowing investigation of wavelength-dependent phenomena in our sample. Inspection of the data shows that the amplitude of variability for each source can indeed vary significantly across the five PS1-MDS filters. Because our initial period-finding analysis assumes a common amplitude across all filters, to estimate filter-specific amplitudes we re-fit the final sample of rotators with a simple sinusoidal model, this time allowing the amplitude in each band to vary independently. Figure 10 shows an example of a light curve

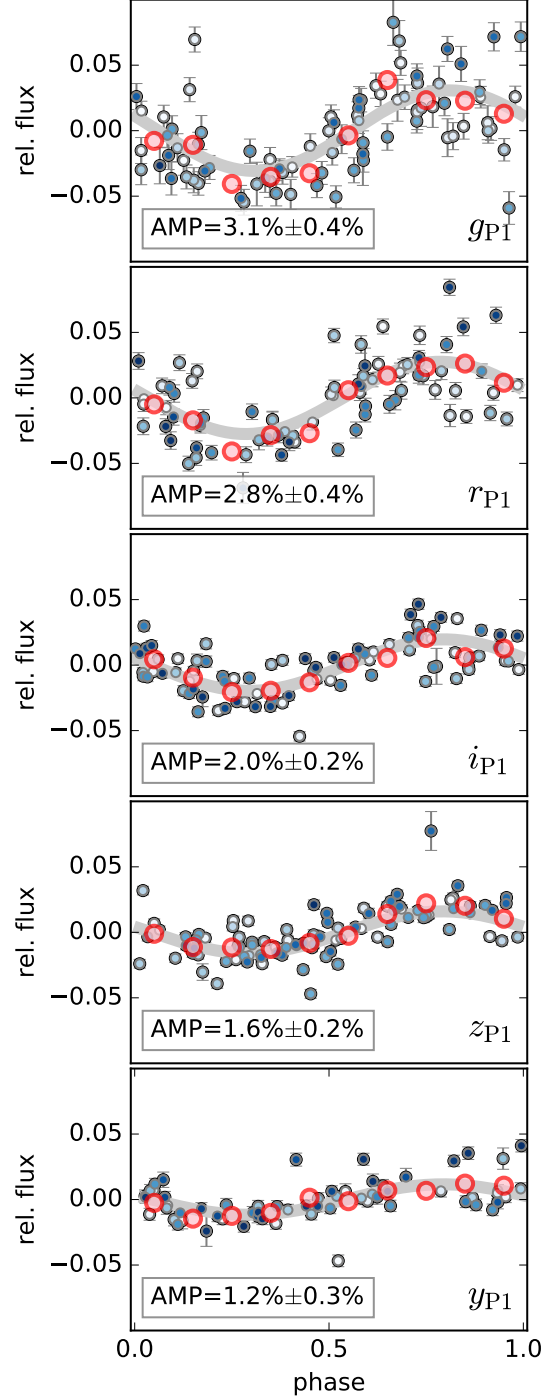


Figure 10. The phased light curve of WISEA J222234.93–001655.4 ($P_{\text{rot}} = 1.87$ days) with the amplitude of variability for each filter allowed to vary. The semi-amplitude of each filter is shown in the bottom left corner of each panel. The points show the phased light curve of the source, colored by time of observation. As in Figure 6, the purple points show the binned mean flux to guide the eye. The model for each filter is shown by the gray curve in each panel. The drop in amplitude is significant between all filters except between g_{P1} to r_{P1} .

with a significant change in amplitude of variability

as a function of filter. The best-fit rotation period of WISEA J105130.40+572218.9 is consistent across all filters at 2.31 days. The amplitude of variability, however, ranges from $1.16\% \pm 0.26\%$ in y_{P1} to $3.08\% \pm 0.41\%$ in r_{P1} . Across the final sample, 248 out of the 271 stars have significant drops in amplitude from r_{P1} to y_{P1} , with the majority following the trend of decreasing amplitude in the redder bands. These findings are consistent with the interpretation that the periodic modulations in our sample of M dwarf light curves are caused by starspots with effective temperatures lower than that of the stellar photosphere (Amado et al. 2000). Due to the red colors of the sources, however, the *absolute* variability amplitudes in the redder bands tend to be greater than those in the bluer bands.

5.5. X-ray Activity

Figure 11 shows the relationship between rotation and X-ray activity in our sample and compares it to a subset of stars from the compilation of Wright et al. (2011). In particular, we show only stars cataloged being field objects with estimated masses $<0.6 M_{\odot}$. The relation between rotation and X-ray activity past the fully-

convective boundary is of particular interest, and is one where our data set is particularly valuable. While the full catalog of Wright et al. (2011) includes 824 stars, only 178 of these are field objects with estimated masses $<0.35 M_{\odot}$. Our work contributes 16 such objects.

Rotation/activity analyses often quantify rotation using the Rossby number $Ro \equiv P_{\text{rot}}/\tau_c$, where τ_c is nominally a turnover timescale associated with convective fluid motions in a star. However, in practice τ_c is determined by evaluating a function of other stellar parameters that is tuned to reduce the scatter observed in rotation/activity relations, so its use injects an ill-defined model dependence into subsequent analysis (cf. Reiners et al. 2014). We therefore simply quantify rotation with P_{rot} . If we reproduce Figure 11 using Ro to quantify rotation, no trends in the data emerge.

Quantifying X-ray activity with L_X/L_{bol} , rather than L_X , injects an additional model dependence into our analysis, since $L_X/L_{\text{bol}} = f_X/f_{\text{bol}}$ depends on our computation of the z_{P1} -band bolometric correction factor $BC_{z,P1}$. However, L_X is a less ideal choice in this case since computing it requires distance measurements, which in our sample are less accurate estimates based on color-magnitude relations.

Table 5. Rotators with Archival X-Ray Detections

Name	X-Ray Name	Mass (M_{\odot})	P_{rot} (day)	$\Delta\theta$ (arcsec)	f_X ($\text{erg s}^{-1} \text{cm}^{-2}$)	$\log_{10} L_X/L_{\text{bol}}$ (dex)
(1)	(2)	(3)	(4)	(5)	(6)	(7)
WISEA J021823.69-044932.5	3XMM J021823.6-044931	0.21 ± 0.04	13.37 ± 0.03	1.2	$(7 \pm 3) \times 10^{-15}$	-2.4 ± 0.3
WISEA J021907.51-033114.2	2XLSSd J021907.5-033114	0.17 ± 0.03	12.38 ± 0.03	0.6	$(3.2 \pm 1.0) \times 10^{-15}$	-3.1 ± 0.2
WISEA J022042.16-030701.0	3XMM J022042.0-030705	0.40 ± 0.07	2.195 ± 0.003	5.1	$(1.4 \pm 0.9) \times 10^{-14}$	-2.7 ± 0.5
WISEA J022121.80-043127.9	2XLSSd J022121.7-043129	0.27 ± 0.05	1.3370 ± 0.0003	1.7	$(2.1 \pm 0.6) \times 10^{-15}$	-3.30 ± 0.10
WISEA J022327.16-052055.0	2XLSSd J022326.9-052056	0.30 ± 0.05	4.019 ± 0.003	3.2	$(4.3 \pm 1.0) \times 10^{-15}$	-3.3 ± 0.2
WISEA J022411.77-041527.7	3XMM J022411.8-041527	0.23 ± 0.04	1.3451 ± 0.0010	1.8	$(1.3 \pm 0.8) \times 10^{-15}$	-3.1 ± 0.4
WISEA J022511.68-050503.2	3XMM J022511.6-050503	0.25 ± 0.04	2.054 ± 0.002	0.4	$(4 \pm 2) \times 10^{-15}$	-3.2 ± 0.3
WISEA J084921.27+444949.2	CXO J084921.2+444949	0.25 ± 0.05	2.3399 ± 0.0010	0.2	$(3.7 \pm 0.7) \times 10^{-15}$	-2.87 ± 0.08
WISEA J095900.97+020830.5	CXO J095900.9+020830	0.48 ± 0.09	2.1793 ± 0.0008	0.1	$(6.1 \pm 0.9) \times 10^{-15}$	-2.74 ± 0.06
WISEA J095918.34+024304.8	CXO J095918.3+024305	0.65 ± 0.10	1.4502 ± 0.0004	0.5	$(1.0 \pm 0.3) \times 10^{-14}$	-2.89 ± 0.10
WISEA J100052.90+015714.1	CXO J100052.9+015714	0.10 ± 0.02	23.61 ± 0.10	0.4	$(5.3 \pm 0.8) \times 10^{-15}$	-2.53 ± 0.07
WISEA J104541.81+592041.1	CXO J104541.9+592040	0.20 ± 0.04	30.8 ± 0.2	1.1	$(4.2 \pm 1.0) \times 10^{-15}$	-3.2 ± 0.2
WISEA J104633.88+574103.6	3XMM J104634.0+574103	0.32 ± 0.06	8.77 ± 0.02	1.2	$(4 \pm 2) \times 10^{-14}$	-2.4 ± 0.4
WISEA J104946.22+573026.7	3XMM J104946.1+573030	0.27 ± 0.05	0.7239 ± 0.0002	3.3	$(1.6 \pm 0.8) \times 10^{-14}$	-2.1 ± 0.4
WISEA J105130.40+572218.9	3XMM J105130.3+572219	0.44 ± 0.08	2.313 ± 0.002	0.3	$(4.6 \pm 1.0) \times 10^{-15}$	-2.93 ± 0.10
WISEA J105633.65+574054.5	3XMM J105633.4+574052	0.48 ± 0.09	1.8020 ± 0.0010	2.5	$(6 \pm 2) \times 10^{-15}$	-2.7 ± 0.2
WISEA J141821.72+522955.2	CXO J141821.7+522955	0.19 ± 0.04	1.5998 ± 0.0005	0.4	$(4 \pm 2) \times 10^{-15}$	-2.7 ± 0.3
WISEA J160956.04+543646.9	CXO J160956.0+543646	0.23 ± 0.04	48.7 ± 0.4	0.1	$(9 \pm 4) \times 10^{-16}$	-3.5 ± 0.3
WISEA J161112.96+541508.3	3XMM J161112.8+541508	0.25 ± 0.04	15.14 ± 0.04	1.0	$(2.5 \pm 1.0) \times 10^{-14}$	-1.9 ± 0.3
WISEA J221509.36+004357.4	3XMM J221509.2+004356	0.16 ± 0.03	1.1948 ± 0.0002	1.8	$(1.6 \pm 1.0) \times 10^{-14}$	-2.6 ± 0.5
WISEA J221513.23-004829.3	CXO J221513.1-004829	0.51 ± 0.09	1.372 ± 0.004	0.7	$(2.1 \pm 0.5) \times 10^{-14}$	-2.50 ± 0.10
WISEA J221722.17-002632.9	3XMM J221722.1-002633	0.09 ± 0.02	2.401 ± 0.002	0.8	$(1.7 \pm 1.0) \times 10^{-14}$	-2.2 ± 0.4

NOTE—Column (5) is the separation between the PS1-MDS source position and the cataloged X-ray position. Column (6) is the X-ray flux in the 0.2–2 keV band.

Figure 11 is notable for showing no clear relation between rotation and activity in our sample, even

though our data span nearly two orders of magnitude in rotation period. However, our sample is

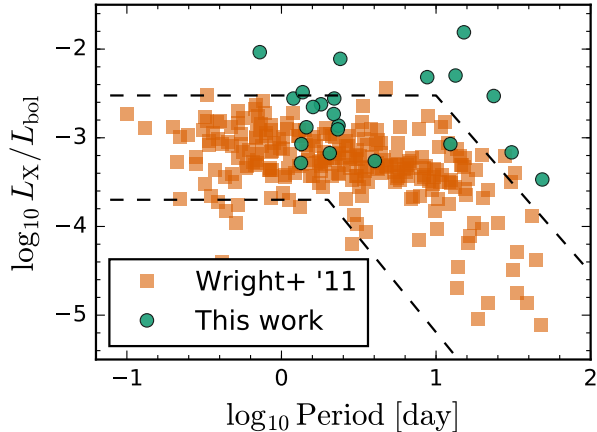


Figure 11. Relation between rotation and X-ray activity for our sample, compared to comparable data from Wright et al. (2011). Dashed lines: approximate envelope of the L_X/L_{bol} vs. P_{rot} relationship observed by Wright et al. (2011).

strongly biased because it contains no X-ray nondetections by construction. Given the characteristically large distances of our targets, only the X-ray brightest of them will have been detected in our catalog search. The source with the largest observed L_X/L_{bol} , WISEA J161112.96+541508.3 ($P_{\text{rot}} = 15.1$ d), does not otherwise appear unusual. While it is not flagged as an X-ray variable in its 3XMM-DR5 catalog record, it was detected in just two separate XMM observations separated by ~ 40 days and so could plausibly have been observed during flares, implying a true quiescent flux lower than what is cataloged. The slowest-rotating target with an X-ray detection, WISEA J160956.04+543646.9 ($P_{\text{rot}} = 48.7$ d), is a weak detection with $f_X = (8 \pm 4) \times 10^{-16}$ erg s $^{-1}$ cm $^{-2}$. Its estimated Rossby number is ≈ 0.6 , placing it in the “unsaturated” regime of the standard rotation/activity relation (Wright et al. 2011) but not in a location that makes its X-ray brightness unusual.

6. CONCLUSIONS

We have measured the rotation periods of 271 cool stars in the PS1-MDS footprint, making a substantial contribution to the overall sample of fully-convective dwarfs with measured photometric rotation periods.

The PS1-MDS data set has strengths that differentiate it from the other data sets used to perform comparable studies. Because our photometry spans five filters, we can winnow a large (~ 4 million source) input catalog to a tractable list of sources of interest, as well as study the wavelength-dependence of the photospheric structures that lead to periodic variability and search for objects that are unusual in this regard. Moreover, because the MDS pointings overlap various fields with deep multiwavelength coverage (GOODS-South,

the Lockman Hole, etc.), large amounts of potentially useful archival data are publicly available. We demonstrated this approach via a cross-match of our catalog to several well-known X-ray catalogs, finding 22 matches; the effort here, however, just scratches the surface of what is possible. In the more distant future, comparable analysis of the LSST data stream (Ivezic et al. 2008) will yield a sample of stellar rotators orders of magnitude larger than the one presented here, allowing true statistical analysis of the relationship between rotation and other parameters in cool field dwarfs.

To enable basic comparisons to prior work, we have extended the technique of Mann et al. (2015, 2016) to develop new polynomials relating PS1 colors to stellar properties and applied these relations to our targets. Now that these stars have been identified as being of unusual interest, it would be valuable to characterize them more precisely and accurately. Both archival investigations and targeted follow-up are underway.

In this work we have focused on developing a catalog of sources that can be confidently identified as cool dwarfs with periodic photometric variability. We have *not* attempted to characterize the sensitivity of our search in detail, nor have we attempted to search for potentially-interesting but marginal candidates. The foundation of such detailed characterization will be a robust, well-understood photometric extraction pipeline, and we therefore defer such work until the final “PV3” reprocessing of the MDS nightly stacks has been performed, at which point we will re-run our search. Final classification of variables will be fully automated to allow us to characterize the search’s sensitivity through simulations.

Although neither our search sensitivity nor the parameters of our targets are fully characterized, the catalog presented in this work shows several interesting features. First, we find tentative evidence that *Kepler* searches for photometric rotation periods are systematically insensitive to objects with $P_{\text{rot}} > 70$ d, as suggested by Newton et al. (2016). Second, we note a dearth of low-mass ($< 0.25 M_{\odot}$) objects with intermediate (~ 10 – 40 d) rotation periods and low ($< 2\%$) variability semi-amplitudes. If the overall lack of such objects is indeed due to a rapid evolution at intermediate (2–5 Gyr; Newton et al. 2016) ages, this suggests that such transitional objects have relatively large, nonaxisymmetric photospheric structures. This may be consistent with the emergence of a less-complex magnetic topology, as proposed by Garraffo et al. (2015) to explain a similar “period gap” in young stars.

Acknowledgments. We thank Elisabeth Newton for her insight into the MEarth dataset. This work was

supported in part by the National Science Foundation REU and Department of Defense ASSURE programs under NSF Grant no. 1262851 and by the Smithsonian Institution.

The Pan-STARRS1 Surveys (PS1) have been made possible through contributions of the Institute for Astronomy, the University of Hawaii, the Pan-STARRS Project Office, the Max-Planck Society and its participating institutes, the Max Planck Institute for Astronomy, Heidelberg and the Max Planck Institute for Extraterrestrial Physics, Garching, The Johns Hopkins University, Durham University, the University of

Edinburgh, Queen’s University Belfast, the Harvard-Smithsonian Center for Astrophysics, the Las Cumbres Observatory Global Telescope Network Incorporated, the National Central University of Taiwan, the Space Telescope Science Institute, the National Aeronautics and Space Administration under Grant No. NNX08AR22G issued through the Planetary Science Division of the NASA Science Mission Directorate, the National Science Foundation under Grant No. AST-1238877, the University of Maryland, and Eotvos Lorand University (ELTE) and the Los Alamos National Laboratory.

REFERENCES

- Ahn, C. P., Alexandroff, R., Allende Prieto, C., et al. 2012, *ApJS*, **203**, 21
- Amado, P. J., Doyle, J. G., & Byrne, P. B. 2000, *MNRAS*, **314**, 489
- Bertin, E. 2011, in *Astronomical Society of the Pacific Conference Series*, Vol. 442, *Astronomical Data Analysis Software and Systems XX*, 435
- Bertin, E., & Arnouts, S. 1996, *A&AS*, **117**, 393
- Bessell, M. S., & Brett, J. M. 1988, *PASP*, **100**, 1134
- Brown, T. M., Latham, D. W., Everett, M. E., & Esquerdo, G. A. 2011, *AJ*, **142**, 112
- Browning, M. K. 2008, *The Astrophysical Journal*, **676**, 1262
- Browning, M. K., Basri, G., Marcy, G. W., West, A. A., & Zhang, J. 2010, *AJ*, **139**, 504
- Chabrier, G., & Baraffe, I. 2000, *ARA&A*, **38**, 337
- Charbonneau, P. 2014, *ARA&A*, **52**, 251
- Chiappetti, L., Clerc, N., Picaud, F., et al. 2013, *MNRAS*, **429**, 1652
- Cook, B. A., Williams, P. K. G., & Berger, E. 2014, *ApJ*, **785**, 10
- Covey, K. R., Agüeros, M. A., Law, N. M., et al. 2016, *ApJ*, **822**, 81
- Cutri, R. M., Wright, E. L., Conrow, T., et al. 2013
- Dittmann, J. A., Irwin, J. M., Charbonneau, D., & Newton, E. R. 2016, *ApJ*, **818**, 153
- Dobler, W., Stix, M., & Brandenburg, A. 2006, *The Astrophysical Journal*, **638**, 336
- Dressing, C. D., & Charbonneau, D. 2013, *ApJ*, **767**, 95
- Evans, I. N., Primi, F. A., Glotfelty, K. J., et al. 2010, *ApJS*, **189**, 37
- Finkbeiner, D. P., Schlafly, E. F., Schlegel, D. J., et al. 2016, *ApJ*, **822**, 66
- Foreman-Mackey, D., Hogg, D. W., Lang, D., & Goodman, J. 2013, *PASP*, **125**, 306
- Garraffo, C., Drake, J. J., & Cohen, O. 2015, *ApJL*, **807**, L6
- Gastine, T., Duarte, L., & Wicht, J. 2012, *A&A*, **546**, A19
- Gizis, J. E., Reid, I. N., & Hawley, S. L. 2002, *AJ*, **123**, 3356
- Green, G. M., Schlafly, E. F., Finkbeiner, D. P., et al. 2015, *ApJ*, **810**, 25
- Irwin, J., Berta, Z. K., Burke, C. J., et al. 2011, *ApJ*, **727**, 56
- Ivezic, Z., Tyson, J. A., Abel, B., et al. 2008, *Living document*, [arxiv:0805.2366](https://arxiv.org/abs/0805.2366)
- James, D. J., Jardine, M. M., Jeffries, R. D., et al. 2000, *MNRAS*, **318**, 1217
- Johns-Krull, C. M., & Valenti, J. A. 1996, *ApJL*, **459**, L95
- Kaiser, N., Burgett, W., Chambers, K., et al. 2010, in *Society of Photo-Optical Instrumentation Engineers (SPIE) Conference Series*, Vol. 7733, *Society of Photo-Optical Instrumentation Engineers (SPIE) Conference Series*, 0
- Kiraga, M., & Stepien, K. 2007, *AcA*, **57**, 149
- Kowalski, A. F., Hawley, S. L., Hilton, E. J., et al. 2009, *AJ*, **138**, 633
- Kraus, A. L., & Hillenbrand, L. A. 2007, *AJ*, **134**, 2340
- Lang, D. 2014, *AJ*, **147**, 108
- Lawrence, A., Warren, S. J., Almaini, O., et al. 2007, *MNRAS*, **379**, 1599
- Li, J., Smith, M. C., Zhong, J., et al. 2016, *ApJ*, **823**, 59
- Magnier, E. 2006, in *The Advanced Maui Optical and Space Surveillance Technologies Conference*, 50
- Mamajek, E. E. 2012, *ApJL*, **754**, L20
- Mann, A. W., Feiden, G. A., Gaidos, E., Boyajian, T., & Braun, K. 2015, *ApJ*, **804**, 64
- . 2016, *ApJ*, **819**, 87
- McQuillan, A., Aigrain, S., & Mazeh, T. 2013, *MNRAS*, **432**, 1203
- McQuillan, A., Mazeh, T., & Aigrain, S. 2014, *ApJS*, **211**, 24
- Meibom, S., Mathieu, R. D., Stassun, K. G., Liebesny, P., & Saar, S. H. 2011, *ApJ*, **733**, 115
- Meisner, A. M., Lang, D., & Schlegel, D. J. 2016, *preprint*, [arxiv:1603.05664](https://arxiv.org/abs/1603.05664)
- Morganson, E., Green, P. J., Anderson, S. F., et al. 2015, *ApJ*, **806**, 244
- Newton, E. R., Irwin, J., Charbonneau, D., et al. 2016, *ApJ*, **821**, 93
- Ochsenbein, F., Bauer, P., & Marcout, J. 2000, *A&AS*, **143**, 23
- Pallavicini, R., Golub, L., Rosner, R., et al. 1981, *ApJ*, **248**, 279
- Pecaut, M. J., & Mamajek, E. E. 2013, *ApJS*, **208**, 9
- Pizzolato, N., Maggio, A., Micela, G., Sciortino, S., & Ventura, P. 2003, *A&A*, **397**, 147
- Reiners, A., & Basri, G. 2010, *ApJ*, **710**, 924
- Reiners, A., Basri, G., & Browning, M. 2009, *ApJ*, **692**, 538
- Reiners, A., Schuessler, M., & Passetger, V. M. 2014, *ApJ*, **794**, 144
- Rest, A., Stubbs, C., Becker, A. C., et al. 2005, *ApJ*, **634**, 1103
- Rest, A., Scolnic, D., Foley, R. J., et al. 2014, *ApJ*, **795**, 44
- Rosen, S. R., Webb, N. A., Watson, M. G., et al. 2016, *A&A*, **560**, 1
- Schlafly, E. F., & Finkbeiner, D. P. 2011, *ApJ*, **737**, 103
- Skrutskie, M. F., Cutri, R. M., Stiening, R., et al. 2006, *AJ*, **131**, 1163
- Tonry, J. L., Stubbs, C. W., Lykke, K. R., et al. 2012, *ApJ*, **750**, 99
- VanderPlas, J. T., & Ivezić, Ž. 2015, *ApJ*, **812**, 18
- Vaughan, A. H., & Preston, G. W. 1980, *PASP*, **92**, 385
- Vauglin, I., Paturel, G., Borsenberger, J., et al. 1999, *A&A*, **135**, 133
- Vilhu, O. 1984, *A&A*, **133**, 117

Wright, N. J., Drake, J. J., Mamajek, E. E., & Henry, G. W.

2011, *ApJ*, 743, 48

Yadav, R. K., Christensen, U. R., Morin, J., et al. 2015, *ApJL*, 813, L31

APPENDIX

A. ESTIMATING M DWARF PARAMETERS FROM PS1 PHOTOMETRY

Here we provide a more detailed description of our method for determining M dwarf stellar parameters from their PS1 photometry (Section 4.1).

Mann et al. (2015) provide relations between SDSS *griz* photometry and fundamental properties of M dwarfs (e.g., T_{eff} , R_*) based on a sample of 183 nearby M dwarfs with precise parallaxes and flux-calibrated optical and NIR spectra. It is possible to convert these to relations to PS1 photometry using the transformations in Tonry et al. (2012). However, the majority of the sample in this paper has $(r-i)_{\text{P1}} > 1$, while only a small fraction of the SEDs used to derive the SDSS–PS1 transformations in Tonry et al. (2012) are this red. Instead we derive new relations using synthetic PS1 magnitudes. We convolve the filter profiles from Tonry et al. (2012) with the Mann et al. (2015) spectra and convert the resulting fluxes to PS1 magnitudes using the appropriate zero points and “tweaks” (used to force agreement between PS1 photometry and spectroscopic standards) from Tonry et al. (2012). We then derive new polynomial relations between T_{eff} , $BC_{z,\text{P1}}$, $M_{z,\text{P1}}$, and M_* and our synthetic $(g-i)_{\text{P1}}$, $(r-i)_{\text{P1}}$, $(i-z)_{\text{P1}}$, or $(r-y)_{\text{P1}}$ colors. Additional terms are added to the polynomial relations as long as they are justified by an F-test. To help account for systematics due to metallicity we also derive relations that include $(g-r)_{\text{P1}}$ in addition to one of the above colors for all physical properties except $BC_{z,\text{P1}}$, which shows negligible improvement from the additional term. We note that these color combinations are imperfect measures of [Fe/H] and the relations likely still have systematics with metallicity.

Table A1. Coefficients for Estimating Stellar Properties

y	Unit	C_a	$C_{a,\text{min}}$	$C_{a,\text{max}}$	C_b	a_0	a_1	a_2	a_3	a_4	b_1	b_2	Scatter	
(1)	(2)	(3)	(4)	(5)	(6)	(7)	(8)	(9)	(10)	(11)	(12)	(13)	(14)	
T_{eff}	3500 K	$(g-i)_{\text{P1}}$	1.6	3.5		2.309	-1.3338	0.5498	-0.119	0.01029			55.	
		$(r-i)_{\text{P1}}$	0.5	2.0		1.483	-0.9843	0.8204	-0.3733	0.06376			56.	
		$(i-z)_{\text{P1}}$	0.3	1.0		1.567	-2.3613	3.928	-3.5069	1.191			59.	
		$(r-y)_{\text{P1}}$	0.9	3.5		1.508	-0.5887	0.271	-0.0682	0.006544			58.	
		$(g-i)_{\text{P1}}$	1.6	3.5	$(g-r)_{\text{P1}}$	2.1	-0.6569	0.1422	-0.01241		-0.3722	0.1702	53.	
		$(r-i)_{\text{P1}}$	0.5	2.0	$(g-r)_{\text{P1}}$	2.094	-0.4136	0.1308	-0.02019		-1.153	0.4175	53.	
		$(i-z)_{\text{P1}}$	0.3	1.0	$(g-r)_{\text{P1}}$	2.186	-0.9242	0.577	-0.1625		-1.245	0.452	54.	
		$(r-y)_{\text{P1}}$	0.9	3.5	$(g-r)_{\text{P1}}$	2.061	-0.2177	0.03055	-0.001817		-1.133	0.4164	53.	
Mass	M_{\odot}	$(g-i)_{\text{P1}}$	1.6	3.5		0.05652	1.319	-0.7755	0.1156				0.17 ^a	
		$(r-i)_{\text{P1}}$	0.5	2.0		0.7666	-0.1287	-0.3029	0.1012				0.19 ^a	
		$(i-z)_{\text{P1}}$	0.3	1.0		0.8164	-0.3494	-1.3962	1.041				0.19 ^a	
		$(r-y)_{\text{P1}}$	0.9	3.5		0.7807	-0.075	-0.1147	0.02327				0.19 ^a	
		$(g-i)_{\text{P1}}$	1.6	3.5	$(g-r)_{\text{P1}}$	2.58	0.4904	-0.4053	0.06325		-3.001	1.15	0.17 ^a	
		$(r-i)_{\text{P1}}$	0.5	2.0	$(g-r)_{\text{P1}}$	4.661	-0.2381	-0.1947	0.07523		-5.993	2.298	0.17 ^a	
		$(i-z)_{\text{P1}}$	0.3	1.0	$(g-r)_{\text{P1}}$	5.134	-1.306	0.2464	0.209		-6.393	2.437	0.18 ^a	
		$(r-y)_{\text{P1}}$	0.9	3.5	$(g-r)_{\text{P1}}$	4.448	-0.4573	0.06287	-0.001415		-5.274	2.014	0.18 ^a	
$BC_{z,\text{P1}}$	mag	$(g-i)_{\text{P1}}$	1.6	3.5		-0.28032	0.74917	-0.21769	0.011735				0.041	
		$(r-i)_{\text{P1}}$	0.5	2.0		0.27469	0.39134	-0.23959	0.015105				0.04	
		$(i-z)_{\text{P1}}$	0.3	1.0		0.20833	1.1028	-1.4065	0.25586				0.037	
		$(r-y)_{\text{P1}}$	0.9	3.5		0.25276	0.25951	-0.094812	0.0004336				0.038	
$BC_{r,\text{P1}}$	mag	$(r-y)_{\text{P1}}$	0.9	3.5		0.2528	-0.5874	-0.1209	0.009721				0.03	
$BC_{i,\text{P1}}$	mag	$(r-i)_{\text{P1}}$	0.5	2.0		0.2728	-0.1441	-0.1914	-0.001051				0.047	
$BC_{y,\text{P1}}$	mag	$(r-y)_{\text{P1}}$	0.9	3.5		0.2707	0.3889	-0.11	0.008266				0.03	
$M_{z,\text{P1}}$	mag	$(g-i)_{\text{P1}}$	1.6	3.5		8.116	-4.5982	3.025	-0.4002					0.37
		$(r-i)_{\text{P1}}$	0.5	2.0		6.211	0.7751	1.81	-0.4355					0.41
		$(i-z)_{\text{P1}}$	0.3	1.0		5.969	1.636	8.947	-4.7744					0.42
		$(r-y)_{\text{P1}}$	0.9	3.5		6.046	0.5451	0.6392	-0.0961					0.41
		$(g-i)_{\text{P1}}$	1.6	3.5	$(g-r)_{\text{P1}}$	4.38	-23.51	14.2	-3.309	0.2817	24.89	-9.885		0.36
		$(r-i)_{\text{P1}}$	0.5	2.0	$(g-r)_{\text{P1}}$	-14.26	-3.695	6.901	-3.125	0.5108	32.05	-11.38		0.37
		$(i-z)_{\text{P1}}$	0.3	1.0	$(g-r)_{\text{P1}}$	-15.77	-9.422	33.9	-30.85	9.942	34.79	-12.54		0.36

Table A1 continued

Table A1 (*continued*)

y	Unit	C_a	$C_{a,\min}$	$C_{a,\max}$	C_b	a_0	a_1	a_2	a_3	a_4	b_1	b_2	Scatter
(1)	(2)	(3)	(4)	(5)	(6)	(7)	(8)	(9)	(10)	(11)	(12)	(13)	(14)
		$(r-y)_{P1}$	0.9	3.5	$(g-r)_{P1}$	-16.25	-1.54	1.906	-0.4622	0.03956	35.38	-13.04	0.36

NOTE—Each row provides values for evaluating a polynomial having the form of Equation A1. Columns (4) and (5) give the range of values for which each relation should be used. Column (14) gives the rms scatter of the polynomial fit to the Mann et al. (2015) sample.

^a Scatter is fractional rather than absolute.

In Table A1 we present coefficients for the new polynomials we have derived, where each row corresponds to an equation of the form

$$\frac{y}{\text{Unit}} = \sum_{i \geq 0} a_i \left(\frac{C_a}{\text{mag}} \right)^i + \sum_{i \geq 1} b_i \left(\frac{C_b}{\text{mag}} \right)^i, \quad (\text{A1})$$

and the second term is only included for rows that list the C_b parameter. Note that we always have $b_0 = 0$. The rms scatters of the various polynomial fits to the properties of the Mann et al. (2015) sample are tabulated as well.

To derive parameters for our stars, we used the polynomials that are functions of $(i-z)_{P1}$, using the metallicity-correcting variants that also depend on $(g-r)_{P1}$ for all of the objects in our sample except the two that do not have a measured $(g-r)_{P1}$ color.

Before evaluating these polynomials, we first iteratively estimated each target star’s distance and reddening in the following manner. We derived an initial distance estimate from each star’s reddened PS1 colors by computing its distance modulus $DM \equiv 5 \log_{10}(d/10 \text{ pc})$ from the observed data and our polynomial expression for $M_{z,P1}$. We then estimated its reddening from the 3D dust maps of Green et al. (2015), using the “Argonaut” web service provided by Green et al. (2015) to download the estimated 3D dust distribution for each relevant line of sight. This estimate is expressed as a set of 20 curves sampling the growth of the reddening parameter $E(B-V)$ as a function of distance modulus, each curve representing one sample from the Green et al. (2015) MCMC analysis of the colors and estimated distances of binned groups of stars. For each of the 20 curves we generated 50 samples of $E(B-V)$ by perturbing the DM estimate by a random offset drawn from a Gaussian distribution corresponding to the noise in the $M_{z,P1}$ polynomial relation. In this analysis we used piecewise linear interpolation between the curve sample points because the shape of the $E(B-V)$ growth function was often jagged, leading to poor fits when cubic spline interpolation was used.

Given a value of $E(B-V)$, the reddening in the PS1 filters can be determined by multiplying by one of the constants tabulated by Schlafly & Finkbeiner (2011). For each source of interest, we iteratively computed reddening corrections and distance estimates until the fractional difference between distance moduli estimated in subsequent iterations was less than 0.001. This process converged for all sources for which it was attempted, although in some cases the estimated distance modulus was not in the range indicated as “reliable” in the Green et al. (2015) data set. We used the scatter in the 1000 samples of $E(B-V)$ to determine uncertainties in the derived distances and reddening corrections. In the final catalog the median A_V is 0.04 mag and the 95th percentile is 0.22 mag, and typical distance uncertainties are 20%. While, as discussed in Section 4.3, our procedure will result in $\lesssim \sqrt{2}$ errors for spatially unresolved binaries, these errors are comparable to the overall accuracy of our procedure given the available information.

To compute T_{eff} , M , and f_{bol} , we evaluated the polynomials given above using the dereddened magnitudes. The apparent bolometric magnitudes are converted to fluxes assuming an absolute solar bolometric magnitude of 4.7554 ± 0.0004 mag and solar luminosity of $(3.8270 \pm 0.0014) \times 10^{33} \text{ erg s}^{-1}$ (Mamajek 2012; Pecaut & Mamajek 2013).